Effect of anode porosity and temperature on the performance and lithium plating during fast-charging of lithium-ion cells

David C. Robertson,[1] LeRoy Flores,[1] Alison R. Dunlop,[1] Stephen E. Trask,[1] Francois L. E. Usseglio-Viretta,[2] Andrew M. Colclasure,[2] Zhenzhen Yang,[1] and Ira Bloom[1]

[1]Chemical Sciences and Engineering Division

Argonne National Laboratory

9700 South Cass Avenue

Lemont, IL 60439 USA

[2]Center for Integrated Mobility Sciences

National Renewable Energy Laboratory

Golden, CO 80401 USA

Abstract

Twenty-four, single layer, ca. 32-mAh pouch cells were tested to determine the effect of electrode porosity on lithium plating. Twelve cells contained a graphite electrode with a porosity of 26%, and another twelve cells contained a graphite electrode with 47% porosity. The cells were cycled using a 6-C charge (constant-voltage charge as needed, maintaining 10 minutes total charging time) and a C/2 discharge protocol at temperatures in the range of 20-50°C. C/20 capacity measurements were initially taken every five cycles for the first 25 cycles. After that the frequency of this measurement changed to every 25 cycles. Reference performance tests (RPTs) were conducted every twenty-five cycles at the testing temperature. A macro-homogeneous electrochemical model and microstructure analysis tool set were used to help interpret experimental observations for the effect of anode porosity and ambient temperature on fast charging performance. Comparison between the two also highlighted gaps in current theoretical understanding that need to be addressed in future work.

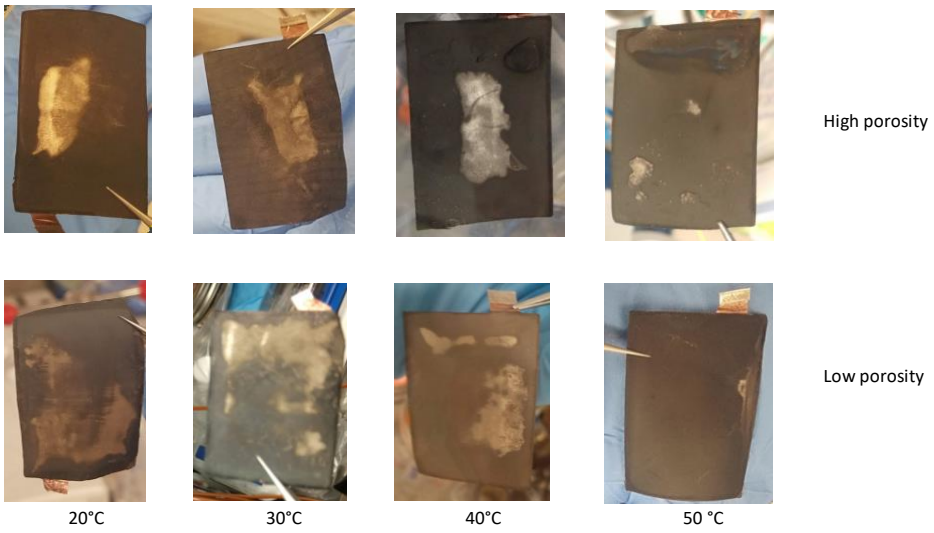

The cells were subjected to post-test examination. Lithium plating was seen in all cells, regardless of porosity. Elevated temperature was shown to reduce the amount of lithium plating and improve initial fast charge capacity, but also changed the rate of other, less well-understood degradation mechanisms. Apparent kinetic rate laws, $At + Bt^{1/2}$, where A and B are constants,

could be fit to most of the capacity loss and resistance increase data. The relative magnitudes of *A* and *B* changed with temperature and porosity. The capacity loss data at 50°C from the high porosity cells were fit by a logistics rate law.

Keywords: *lithium-ion cells; fast charging; electrode porosity; performance degradation*

Introduction

Range anxiety may be a limiting factor in the general acceptance of all-electric vehicles (EVs). The ability to quickly fill or partially recharge the battery pack in the vehicle may allay some of these fears of not having enough energy in the battery to reach a destination. Ideally, the driver of the EV would be able to find a fast-charging station, and, like partially fueling an internal-combustion-engine-powered vehicle, put enough energy into the battery pack in a small amount of time, such as 10 minutes or less, to get to the desired destination. Enabling fast charging of the battery may introduce several life-limiting and, potentially, safety-related issues in lithium-ion technology. Among these is the potential for lithium plating at the graphite, negative electrode during the fast charge process.

Normally, lithium (i.e., Li^+ and 1 e^-) intercalates into graphite in stages.[1-4] As can be expected, this process is limited by diffusion and kinetics. There is a limit to the amount of lithium that can enter the graphite structure, depending on time and temperature. Given this as a background, as the graphite structure fills with lithium, the rate at which it can enter will decrease. If the rate

of lithium transport from the positive electrode to the graphite electrode is faster than lithium diffusion into the graphite structure, metallic lithium may plate on the graphite surface.

If the local potential on the graphite surface is less or equal to 0 V (vs. Li^+/Li), metallic lithium can plate.[5-7] In a full cell, this condition is possible when the cell voltage is 4 V or greater. There are reports that the possibility of plating increases with current density and with decreasing temperatures.[6-11] One simple engineering approach to decrease the local current density would be to increase the specific surface area, S_p, by decreasing the porosity, ε, of the negative electrode according to the analytical relationship, $S_p=3(1-\varepsilon)/r$, with r being the particle radius. This relationship used extensively in battery modeling[12-15] is derived assuming an infinite medium made of non-overlapping spheres with no surface roughness. However, this linear correlation relies on several assumptions that limit its domain of validity, so that the expected impact on current density may be over- or underestimated. The correlation between the porosity and the specific surface area was further investigated by calculations using numerically generated microstructures, which challenged the standard method ($S_p=3(1-\varepsilon)/r$) used to calculated specific surface area in battery macroscale modeling.

We investigated the effect of negative-electrode porosity in two sets of small pouch cells. One set of cells contained negative electrodes with 26% porosity, and the other, 47%. Both were subjected to fast-charging (6-C) cycling protocols at temperatures in the range of 20-50°C. After cycling, post-test examination was performed to determine the efficacy of the experimental condition on lithium plating reduction. A modeling tool set was also used to better understand

the effect of anode porosity changes and operating temperature on initial fast charge capacity and amount of lithium plating.

Other researchers have explored the effect of temperature on lithium plating and shown that elevated temperature significantly reduces lithium plating[16,17]. Modeling based papers have shown an increase in anode porosity should also significantly reduce plating.[18] However, our comprehensive approach of experimental measurements and electrochemical/microstructure modeling show lithium plating is not a strong function of anode porosity. Explanations for this somewhat non-intuitive result are discussed in detail throughout the manuscript. Further, the papers explore the effect of fast charging at elevated temperature on other cell degradation mechanisms. Even though plating is mitigated at elevated temperature, the capacity retention is often worse due to other fade mechanisms.

Experimental

Materials. Twenty-four, single layer, xx3450 pouch cells (ca. 32 mAh) were made by the CAMP[19] Facility at Argonne.[20] The electrodes in the cell measured 34 × 50 mm. The composition of the single-sided electrode laminates is given in Table 1. The negative electrodes for the low porosity graphites were calendered and the negative electrodes for the high porosity graphites remained uncalendered. At the time of the pouch cell build, the measured porosity of the calendered, low porosity graphite was 26%, and that of the uncalendered graphites was 47%. The negative-to-positive ratio was 1.1:1. The electrolyte consisted of 1.2 M $LiPF_6$ in ethylene carbonate:ethylmethyl carbonate (3:7 by weight).

Table 1. Composition of laminates used.

Positive Electrode	Negative Electrode
$Li(Ni_{0.5}Mn_{0.3}Co_{0.2})O_2$ (NMC532)	**SLC1506T**
90 wt% Toda NMC532	91.83 wt% Superior Graphite SLC1506T
5 wt% Timcal C45 carbon	2 wt% Timcal C45 carbon
5 wt% Solvay 5130 PVDF	6 wt% Kureha 9300 PVDF binder
Coating thickness: 71 μm (18.63 mg cm^{-2};	0.17 wt% oxalic acid
35.4% porosity)	Coating thickness: 62 μm (9.94 mg cm^{-2};
Al foil thickness: 20 μm	26.1% porosity) and 87 μm (9.94 mg cm^{-2};
	47% porosity)
	Cu foil thickness: 10 μm

Cell testing. The cells were placed in fixtures, such as that shown in Figure 1. All cells were formed at 30°C by applying a 1.5 V tap charge at a rate of C/10 and held for 15 minutes at 1.5 V, OCV (rest) relaxation wetting period for 12 hours. Following the rest period, the cells were cycled between 3 to 4.1 V for 3 cycles using a constant-current, constant-voltage charge profile (CCCV) consisting of charging at the C/10 rate to 4.1 V and maintaining the potential there until current was less than C/20 rate. The constant-current (CC) discharge part of the cycle consisted of discharging at the C/10 rate to 3 V. Three additional cycles were performed using a CCCV profile, charging at the C/2 rate until a current below C/10 was observed and CC discharge at the C/2 rate. Finally, the cells were put in a safe state by CCCV charging at the C/10 rate to 3.5 V and holding the potential there for 6 hours. The cells were de-gassed and vacuum sealed.

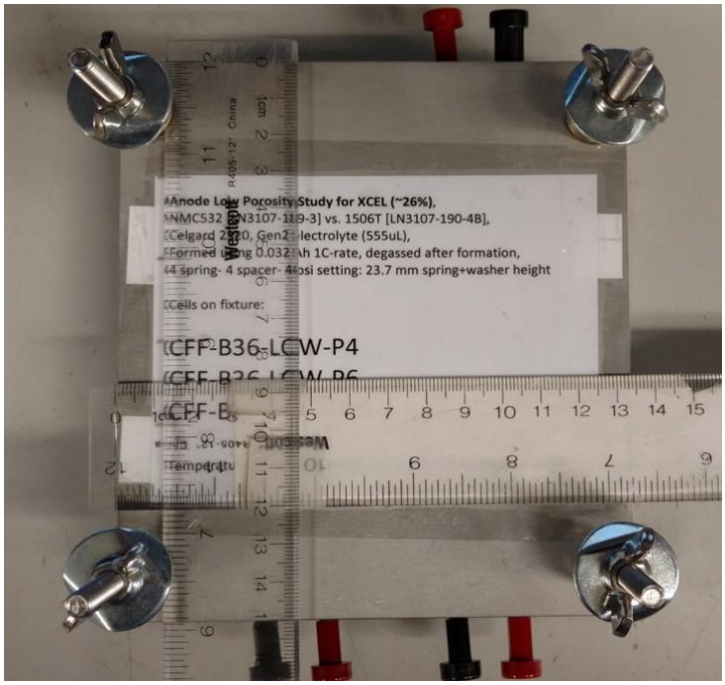

Figure 1. Cell fixture used in the experiment. Each fixture contained three cells and acrylic spacers to both apply stack pressure directly on each cell assembly and evenly distribute the pressure. The applied pressure was approximately 276 mbar (4 psi) per cell.

The cells were heated to the testing temperatures of 20, 30, 40 and 50°C (3 cells each) and allowed to equilibrate for ~ 4h. The cells were characterized in terms of C/20 capacity measurements and the hybrid pulse-power characterization test (HPPC).[21] These measurements, RPT0, served as the bases for gauging performance changes during the cycling portion of the experiment.

The HPPC test was based on that given in the PHEV Battery Test Manual.[21] A 5-C discharge pulse was performed at 100% SOC. Ten percent of the rated capacity was then removed at the

1-C rate. The test then consisted of 10-s discharge and charge pulses at the 3- and 2.2-C rates at every 10% SOC.

The cells were cycled at the test temperature using a 6-C charge plus a constant-voltage hold, as needed, maintaining 10 minutes total charging time, and a C/2 discharge protocol. The voltage limits were 3.0 and 4.1 V. For the first 50 cycles, the cycling protocol included one cycle of discharging and charging at the C/20 rate every fifth cycle. After 50 cycles, the frequency of the C/20 cycles was every 25 cycles. The low-rate cycles were included in the total cycle count.

Reference performance tests (RPTs) were conducted every 25 cycles at the testing temperature. The RPT consisted of the HPPC test.

After 5 cycles, one cell from each test condition was removed and analyzed for physical changes on the graphite anode. The remaining cells accrued 200 cycles. They were then analyzed for physical changes on the anode.

Post-test analysis. All post-test examinations were performed in an argon-atmosphere glove box, which typically contained about 0.1 ppm oxygen and 0.2 ppm water. The cells were cut open using ceramic scissors to avoid shorting. The physical changes were documented by optical photographs.

Data reduction. C/20 capacity values were taken directly from the RPT data. The values of the cell resistance as a function of open-circuit voltage (OCV) and of %SOC were calculated from

the HPPC results. The values of cell resistance at 3.72 V (~60% SOC) were interpolated from these values using the FORECAST function in Microsoft® Excel®.

The relative changes in the performance metrics, C/20 capacity and cell resistance, were analyzed for trends using similar methods. The relative change in the metric was calculated using $\Delta Z = 1 - \frac{Z_i}{Z_{RPT0}}$, where Z_i is the capacity or resistance of the cell at RPT*i*. These values were averaged and trends in the average, relative data were elucidated using the LINEST function in Excel®. The value of ΔZ at RPT0 was defined as zero and was not included in fitting in all cases.

Three forms of Equation 1 were used in curve-fitting for all data sets except that of the capacity data from the high porosity cells tested at 50°C (see below). The forms of Equation 1 can be described as linear-with-time (B=0), parabolic ($t^{1/2}$; A=0), and mixed mechanism (A, $B \neq 0$). The goal of the process was a fit that used the least number of terms and that produced a satisfactory fit, i.e., the value of the regression coefficient, r^2, was greater or equal to 0.95. The fitting process used the averaged values of ΔZ from each temperature independently and used the LINEST function in Microsoft® Excel® to perform the fitting.

$$\widehat{\Delta Z} = At + Bt^{1/2}, \qquad \text{Equation 1}$$

where A and B are fitting constants and t is cycle count. The estimated values of A and B were also examined for trends using Excel®.

The capacity data from the high porosity cells that were tested at 50°C were not amenable to fitting by Eq. 1. Instead, logistics-based, kinetic rate law, Equation 2, was fit to these data.[22]

$$\widehat{\Delta C} = \frac{K}{1+Ae^{-kt}}, \qquad \text{Equation 2}$$

where *K*, *A*, and *k* are fitting constants and *t* is cycle count. The Solver® in Excel® was used to perform the fitting in this case.

Electrochemical modeling and microstructure analysis. A previously reported electrochemical model was used to investigate the effect of anode porosity and temperature on fast charge capacity and lithium plating.[12,13] Parameters for solid-state diffusion and exchange current density of Superior Graphite 1506T and NMC532 at 30°C are reported in Reference 17. Electrolyte transport properties, as a function of local salt concentration and cell temperature, were modeled with the equations reported in Reference 13. Lithium plating and stripping are modeled with the formulation proposed by Ren[23] using an exchange current density of 10 A m^{-2} as estimated in gas titration experiments in conjunction with electrochemical modeling.[24] The activation energy for solid-state diffusivity and intercalation exchange current density are estimated to be 30 kJ mol^{-1} for both graphite and NMC based on high-power current pulses at 20-50°C in a custom reference electrode cell.[25] The cathode film resistance, incorporated into the model, is estimated to be 0.015 Ω-m^2 with an activation energy of 8 kJ mol^{-1} based on electrochemical impedance spectroscopy data and high-current pulse measurements. Previous experiments with similar electrodes/electrolyte showed that the cathode/electrolyte interface degrades at temperatures above 45°C from lack of additives.[26] The model results, shown in

Figure 2, at 50°C are with the cathode film resistance increased four times to 0.06 Ω-m^2. This increased film resistance at 50°C results in a good match between model predictions and experimentally measured fast charge capacity (Figure 2) and cell resistance (Table 2).

A microstructure tool set was used to investigate the impact of porosity changes on microstructure properties, which is critical for understanding how anode porosity variation due to calendering affects fast charge performance. A detailed discussion of the microstructure analysis is given in the supplemental material.

To estimate the effect of anode porosity on fast charge performance, a thorough estimate is needed for the tortuosity factor as function of electrode porosity. The tortuosity is estimated based on analysis of 3D microstructure geometry generated using X-ray computed tomography.[27] The tortuosity has also been directly measured for similar anodes using symmetric cell setup with blocking electrolyte.[27] In this setup, the electrochemical impedance spectrum is measured and fitted to a transmission line model to extract effective ionic conductivity.[28] The tortuosity factor is then deduced from effective ionic conductivity, bulk electrolyte ionic conductivity, and porosity.

By considering microstructure reconstruction estimates, direct tortuosity measurements, and lithium plating observations, the tortuosity for the low and high porosity anode are estimated to be 6.5 and 5.0, respectively. This assumes the representative particle radii for these two anodes are set to 4 and 5 microns, respectively, to take into account the reduction of solid-state diffusion distance induced by particle cracking and particle morphology change triggered by the

calendering step. While the tortuosity factor fitted for the calendered electrode is within the predicted interval from reconstruction (5.3-9.0), the one for the high porosity electrode is significantly higher than expected (2.5-3.3), with the interval being attributed to the carbon/additive uncertainty. This result suggests (i) the impact of the carbon/binder additives on tortuosity is underestimated and (ii) the impact of porosity on tortuosity factor is overestimated, in agreement with experimental measurements[28] for this microstructure. However, if the change in the solid-state characteristic diffusion between the two electrodes is neglected (i.e., 5 μm radius for both uncalendered and calendered electrodes), the assumption of a relatively high tortuosity factor of 6.5 for both electrodes enables similar predictions. For example, similar plating predictions can be achieved by using a higher tortuosity factor (triggers earlier lithium plating) and lower equivalent diameter (delays lithium plating) for the calendered electrode.

The impact of calendering is not limited to the porosity, as particle shape and alignment, crack density, and specific surface area are also modified. In particular, change of particle morphology and particle cracking will reduce the solid-state characteristic diffusion distance, suggesting that keeping constant the particle diameter used in the macroscale model between the two set of electrodes is likely incorrect, especially for the highly calendered electrodes considered in this work. In addition, the analytical relationship used to correlate specific surface area and porosity has a limited range of validity: it is not applicable for the low porosity electrodes, as discussed in the supplemental material. The combination of specific surface area and diameter uncertainty, both known to control lithium plating, may lead to an overfit of the tortuosity factor in the model if only the tortuosity factor, and not all three parameters (S_p, τ, and D_{50}), are allowed to be modified between the low and high porosity electrodes. The same unwanted tortuosity

overfitting can occur if the specific surface area and/or particle diameter are adjusted incorrectly. Because of this, we consider the tortuosity factors of 6.5 and 5.0 to be more plausible, and these are used for the results obtained with the macro-homogeneous model in the rest of the article.

Results

Cell testing. The values of cell capacity and resistance at RPT0 from the cells that went through the cycling test are given in Table 2 and are grouped by test condition. The initial performance of the cells that were removed after 5 cycles was not significantly different from the values in Table 2.

Table 2. Initial values of cell capacity and resistance at the test temperature.*

Electrode type	Temperature, °C	Cell capacity, mAh	Cell resistance, Ω
Low porosity	20	35.09 (0.30)	2.30 (0.14)
	30	36.28 (0.62)	1.93 (0.07)
	40	35.29 (0.18)	1.67 (0.06)
	50	35.32 (0.02)	1.90 (0.05)
High porosity	20	36.30 (0.32)	2.18 (0.37)
	30	37.09 (0.18)	1.93 (0.04)
	40	37.15 (0.15)	1.71 (0.13)
	50	37.56 (0.03)	1.88 (0.17)

*The value in parentheses represents the uncertainty in the reported value. Since there were only two cells per condition in the cycling experiment, the uncertainty was calculated from |(average

value)-(observed value)| for each condition; thus, average+uncertainty and average-uncertainty represent the range of the observed values.

Figure 2 illustrates the fast charge capacity added to cells with low and high porosity anodes during the 10-minute charge protocol of constant current and voltage (CC-CV), implemented for the second cycle at operating temperatures of 20-50°C. The average of measurements for three cells for each condition is plotted as open circles versus electrochemical model simulations, shown as solid lines. The capacity linearly increases with time during CC charging, and the rate of capacity addition decreases during the CV charging due to decreasing current. For the low porosity cell, the average charge capacities achieved in 10 minutes were 20.2, 23.2, 25.2, and 25.7 mAh at 20, 30, 40, and 50°C, respectively. The corresponding capacity values for the high porosity cells were slightly higher, 20.7, 23.6, 26.4, and 26.5 mAh. There was good agreement between measured capacity and the simulation results from the electrochemical model for the chosen parameter set. Increasing the porosity resulted in very little improvement in the 10-minute capacity values compared to those at elevated temperatures. To be discussed below, this behavior seems to be due to the anode tortuosity remaining unexpectantly high even with high porosity and slightly longer solid-state diffusion distance for uncalendered particles.

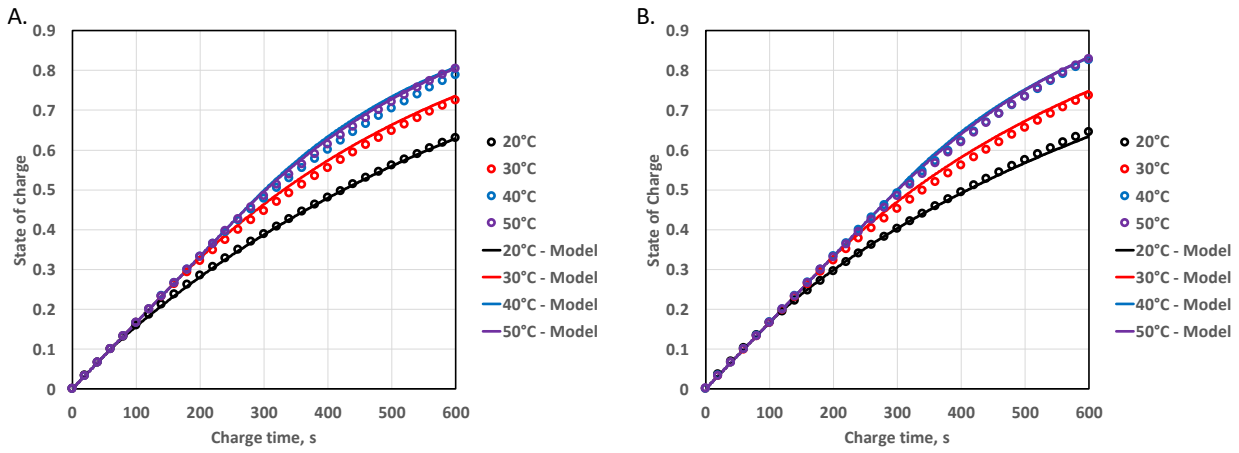

Figure 2. Charge capacity as function of time during initial 10 minute CC-CV charging for low porosity (A) and high porosity (B). The experimental measurements are the average of three cells and are shown as circles. Model results are plotted as solid lines.

Cell performance decreased with cycling at each temperature, as expected. The remaining parts of this section will be divided according to performance parameter, capacity and resistance, for the sake of clarity. Each section will compare the performance of the two types of cells, low porosity and high porosity, as given by the performance metric.

Capacity. Plots of the average, relative change in cell capacity vs. cycle count and the results of fitting for the low porosity cells that accrued 200 cycles are given in Figure 3. From the shape of these curves, it appeared that the data followed the same type of kinetic rate law. Indeed, fitting these data to Equation 1 showed that this was the case. These results are also shown in Figure 3. The values of the fitting coefficients are given in Table 3. The values in Table 3 indicate that the fits were very good. The values also indicate that the linear component of the apparent rate law was small and contributed ~10% or less to the overall rate. Indeed, the

two negative values in Table 3 suggest that there was a linear-with-time process that impeded capacity loss at 30 and 40°C. The nature of this process is not known.

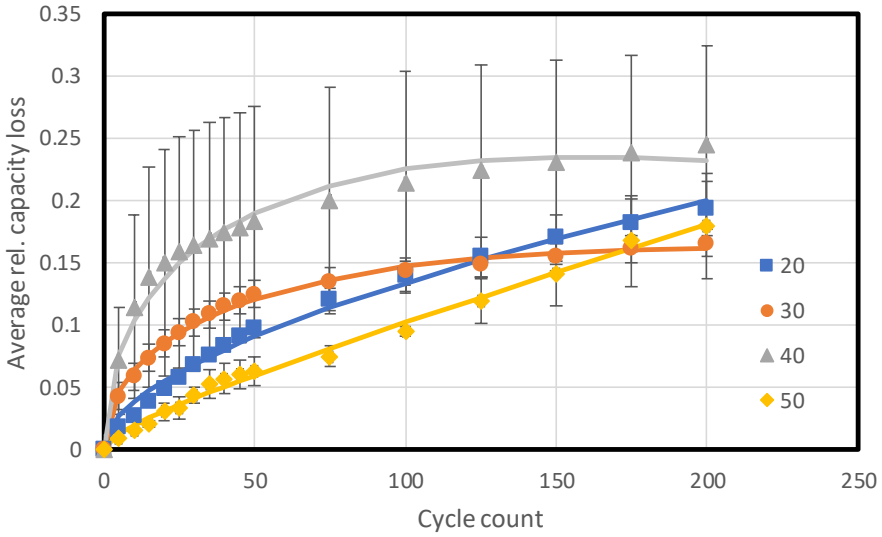

Figure 3. Average, relative capacity loss vs. cycle count for the low porosity cells tested at temperatures of 20, 30, 40 and 50°C. The markers represent the average values and the solid curves, the results of fitting. The error bars represent the range of values; see note under Table 2.

Table 3. Results from fitting Equation 1 to the capacity loss data from the low porosity cells. The value in parentheses is the standard error of the estimate.

Temperature, °C	*A*, $(\text{cycles})^{-1}$	*B*, $(\text{cycles})^{-1/2}$	r^2
20	1.97×10^{-4} (6.12×10^{-5})	1.14×10^{-2} (6.76×10^{-4})	>0.99
30	-7.91×10^{-4} (3.39×10^{-5})	2.26×10^{-2} (3.74×10^{-4})	>0.99
40	-1.48×10^{-3} (9.03×10^{-5})	3.73×10^{-2} (9.97×10^{-4})	>0.99

50	6.14×10^{-4} (4.65×10^{-5})	4.07×10^{-3} (5.13×10^{-4})	>0.99

Plots of average, relative change in cell capacity and the results of fitting for the two cells that completed 200 cycles at each temperature are given in Figures 4(a) and (b) for the high porosity cells. Fitting a single equation to these data was problematic. By inspecting the data in Figures 4(a) and (b), there were two obvious, temperature-dependent processes present, one at the lower temperatures of 20, 30 and 40°C, and another at 50°C. When a rate law of the general type, At^z, were used on the lower-temperature data, the resulting values of z were 0.87, 1.00 and 0.77 for 20, 30 and 40°C, respectively, and the values of r^2 were in the range of 0.94 to 0.96. The values of z indicated that the dependence on time for capacity fade process changed with temperature from one that depended on t and $t^{1/2}$ to just t and back again.[29] Clearly, the capacity fade process was complex.

The values of the fitting coefficients in Equation 1 using the low temperature data are given in Table 4a. The values of the regression coefficient, r^2, indicated that the fits were very good. Least-squares fitting of the values of A and B shows that each set is linear with temperature (r^2 = 0.99 in both cases). From these results, it can be inferred that the processes do not follow Arrhenius-like kinetics.

Equation 2 was fit to the capacity loss data from the 50°C, high porosity cells with a value of r^2 equal to 0.99, as shown in Figure 4b and Table 4b. Instead of the mixed, $t + t^{1/2}$ rate law, a logistics rate law was used. Logistics kinetics are common where there is a reaction which has a limited amount of reaction material. When the limiting material is plentiful, the reaction rate

increases with time, reaching a maximum rate about 90 cycles in this case. After that point, the amount of limiting material decreases sharply, causing a corresponding decrease in observed rate. This type of behavior is usually seen in biological systems where bacteria grow on a limited food supply. In our case, the limiting material may be the amount of active anode material. After a point, chemical and physical stress in the cell may cause binder degradation, limiting the amount available for lithium intercalation.

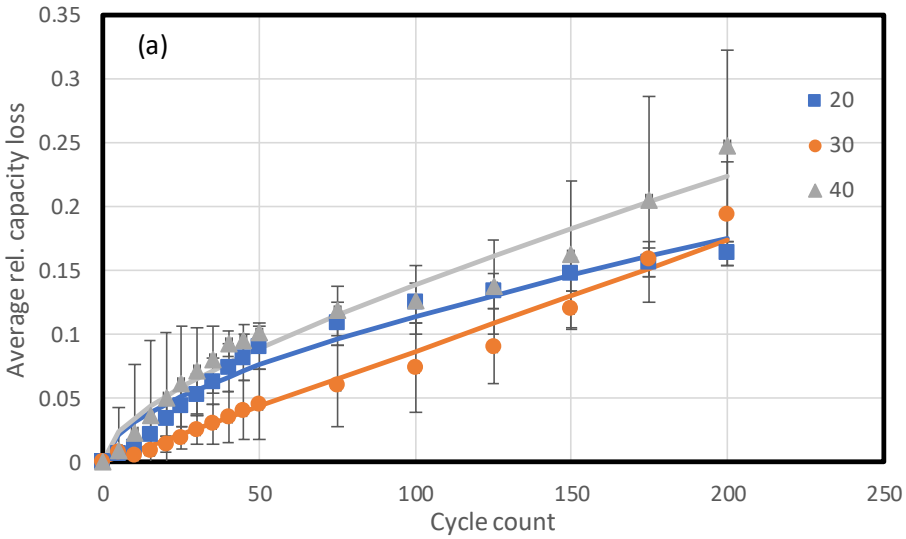

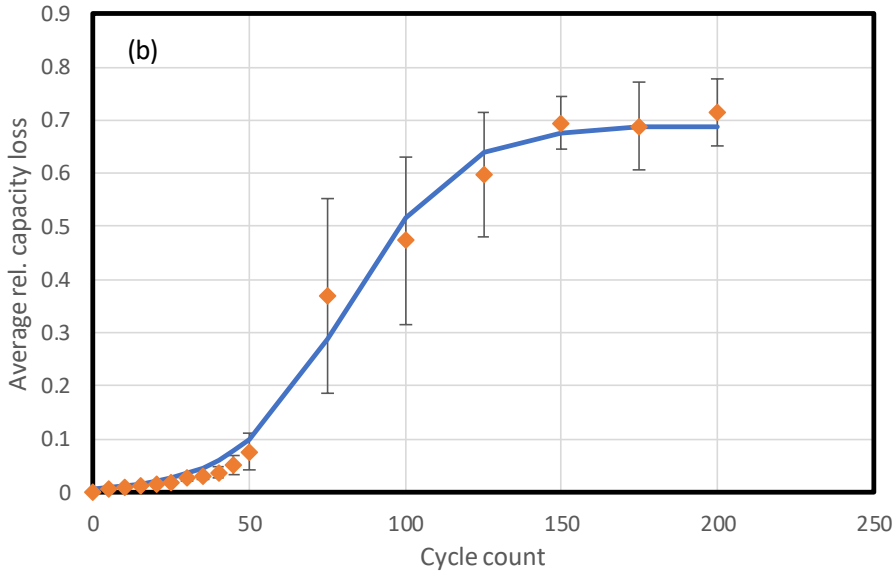

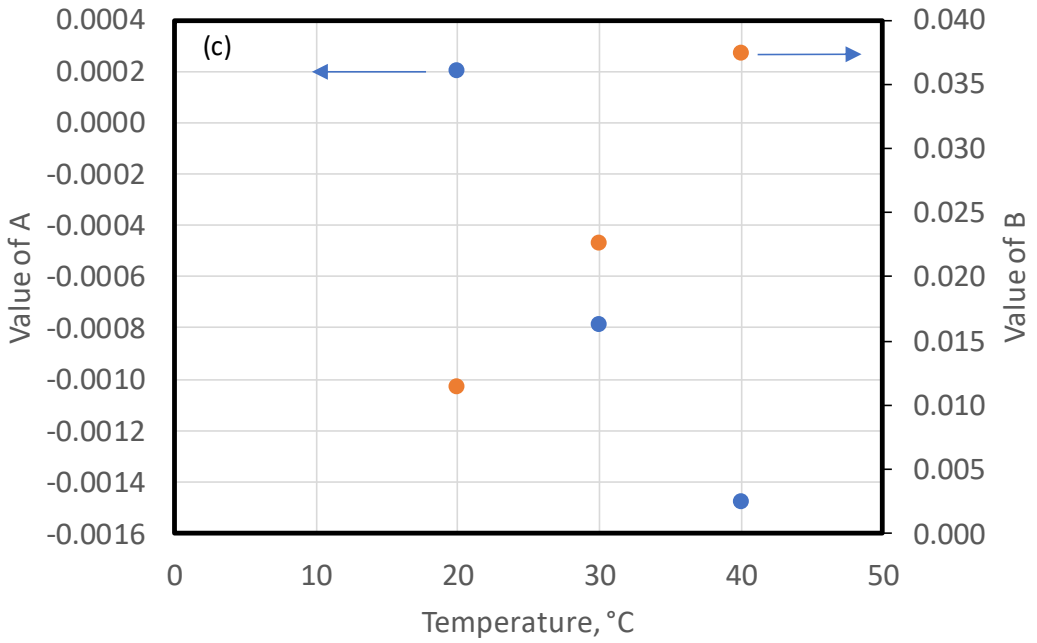

Figure 4. (a) Average, relative capacity loss vs. cycle count for the high porosity cells tested at temperatures of 20, 30 and 40°C. (b) Average, relative capacity loss vs. cycle count for the cells tested at 50°C. The markers represent the average values and the solid curves, the results of fitting. The error bars represent the range of values; see note under Table 2. (c) Values of the fitting parameters A and B vs. temperature. From the least-squares fitting of the low-temperature data, A=-8.39 × 10^{-5}T +1.83 × 10^{-3} and B=1.30 × 10^{-3}T-1.51× 10^{-2}, where T is temperature in °C.

Table 4a. Values of fitting constants for cells tested at 20, 30, and 40°C. The value in parentheses is the standard error of the estimate.

Temperature, °C	A, (cycles)$^{-1}$	B, (cycles)$^{-1/2}$	r^2
20	2.33 × 10^{-4} (1.10 × 10^{-4})	9.08 × 10^{-3} (1.22 × 10^{-3})	0.99

30	8.67×10^{-4} (2.41×10^{-5})	0.00	0.99
40	4.48×10^{-4} (1.34×10^{-4})	9.46×10^{-3} (1.48×10^{-3})	0.99

Table 4b. Values of the fitting coefficients for cells tested at 50°C.

K	*A*	*k*, (cycles)$^{-1}$	r^2
0.69	106.21	5.77×10^{-2}	0.99

Resistance. A plot of the average, relative change in cell resistance vs. cycle count for the low porosity cells is given in Figure 5a along with the fitting results. It should be noted that there were two points in the 50°C data set that were clearly outliers and were excluded from the curve fitting. These two points are shown in Figure 5a above the best-fit curve.

The results of fitting Equation 1 to the data are shown in Table 5. The high values of r^2 indicate that the fits were very good. Examining the data in Table 5 shows that there are significant changes in the apparent rate equation. The rate equation changes from linear-with-time to square-root-of-time to mixed linear and square root with increases in test temperature. Comparing the relative magnitudes of *A* and *B* shows that *A* is about ten times that of *B*. This is also shown in Figure 5b as a plot of the value of the fitting coefficients, *A* and *B*, vs. temperature. The kinetics of resistance increase tend to be more linear-with-time than parabolic.

The negative values of *B* were perplexing. At face value, they imply that there was a process that impeded resistance with time at the higher temperatures. However, if one assumes that

resistance was primarily due to growth of the solid electrolyte interphase (SEI) layer, the nature of this process is not known. The negative values may indicate that a (minor) process is removing or thinning the SEI layer.

Table 5. Results of fitting Equation 1 to the individual data sets.

Temperature, °C	A, $(\text{cycles})^{-1}$	B, $(\text{cycles})^{-1/2}$	r^2
20	0.00	5.90×10^{-4} (7.79×10^{-6})	>0.99
30	1.30×10^{-2} (1.17×10^{-4})	0.00	>0.99
40	6.09×10^{-2} (3.25×10^{-3})	-2.17×10^{-3} (2.73×10^{-4})	>0.99
50	9.55×10^{-2} (5.74×10^{-3})	-3.11×10^{-3} (4.20×10^{-4})	>0.99

Least-squares fitting of the data in Figure 5b shows that the values of A and B change linearly with temperature. The value of A increases with temperature, while the value of B decreases.

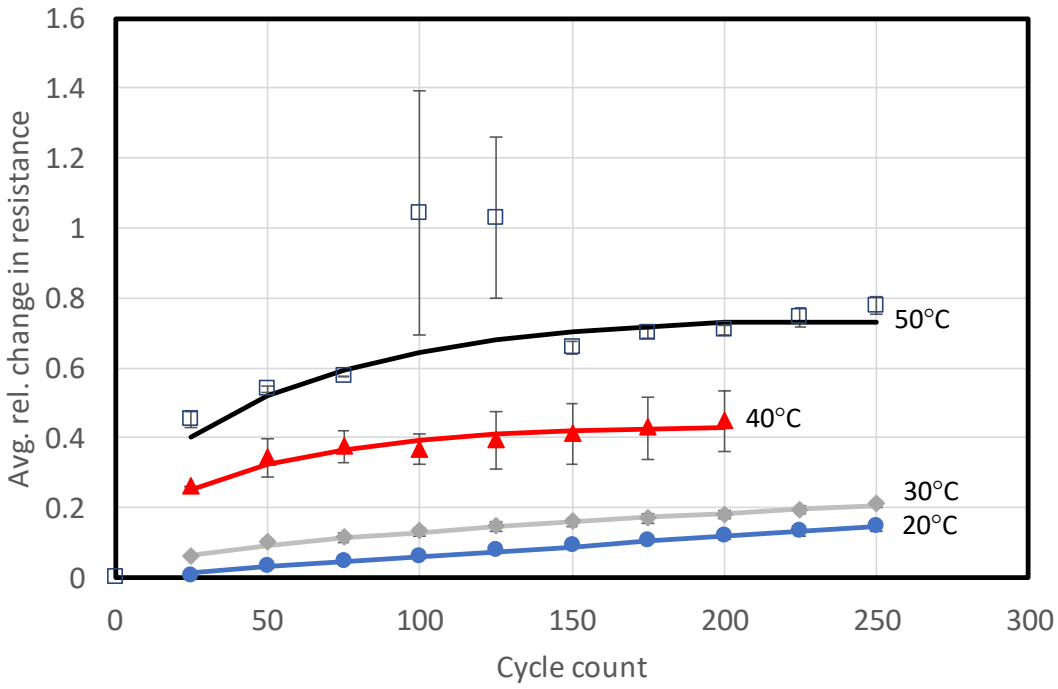

Figure 5a. Average, relative change in cell resistance vs. cycle count for the low porosity cells. The test temperatures are shown next to each data set. The error bars indicate the range of values. If no error bar was visible, then the range of values was smaller than the marker. The two outliers in the 50°C data are most likely due to changes in contact resistance caused by disconnecting and subsequently reconnecting the cell.

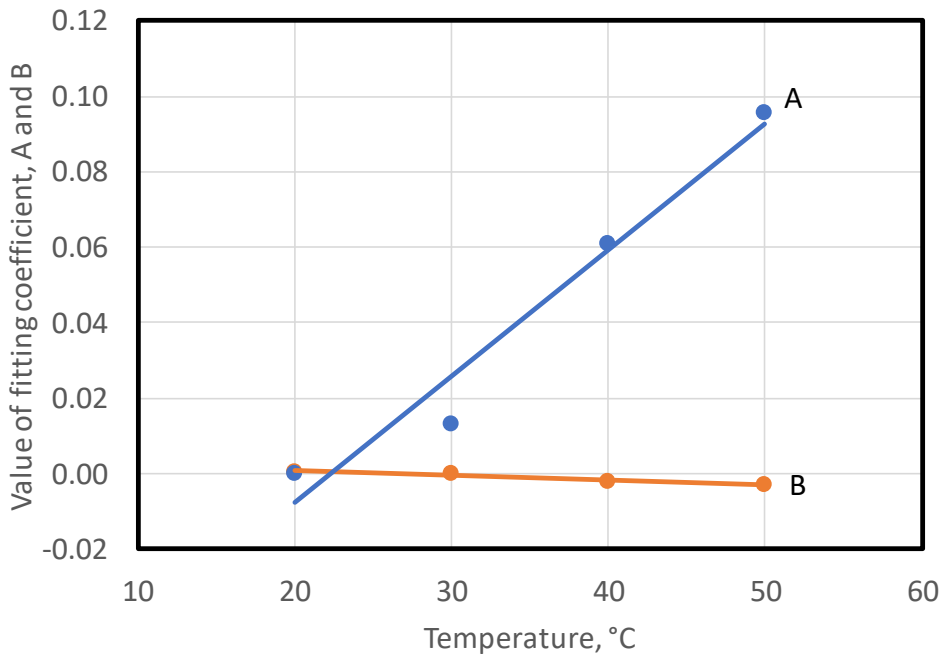

Figure 5b. Value of the fitting coefficients, *A* and *B*, vs. temperature. The markers represent the data and the curve, the results of least-squares fitting. The values of r^2 were in the range of 0.95 to 0.96 in both cases.

A plot of the average, relative change in cell resistance vs. cycle count is given in Figure 6a for the high porosity cells. Fitting Equation 1 to the data in the figure revealed that two mechanisms for resistance increase were present, parabolic (20-40°C) and linear-with-time (50°C). These results are also shown in Figure 6a. The values of the fitting constants, *A* and *B*, are given in Table 6. Based on the r^2 values in Table 6, the fits were very good.

A least-squares fitting of the values of *B* in Table 6 from the 20-40°C cells shows that they depend linearly on temperature (see Figure 6b). The linear temperature dependence of these values is analogous to that seen in the values of the fitting constants from the low porosity cells.

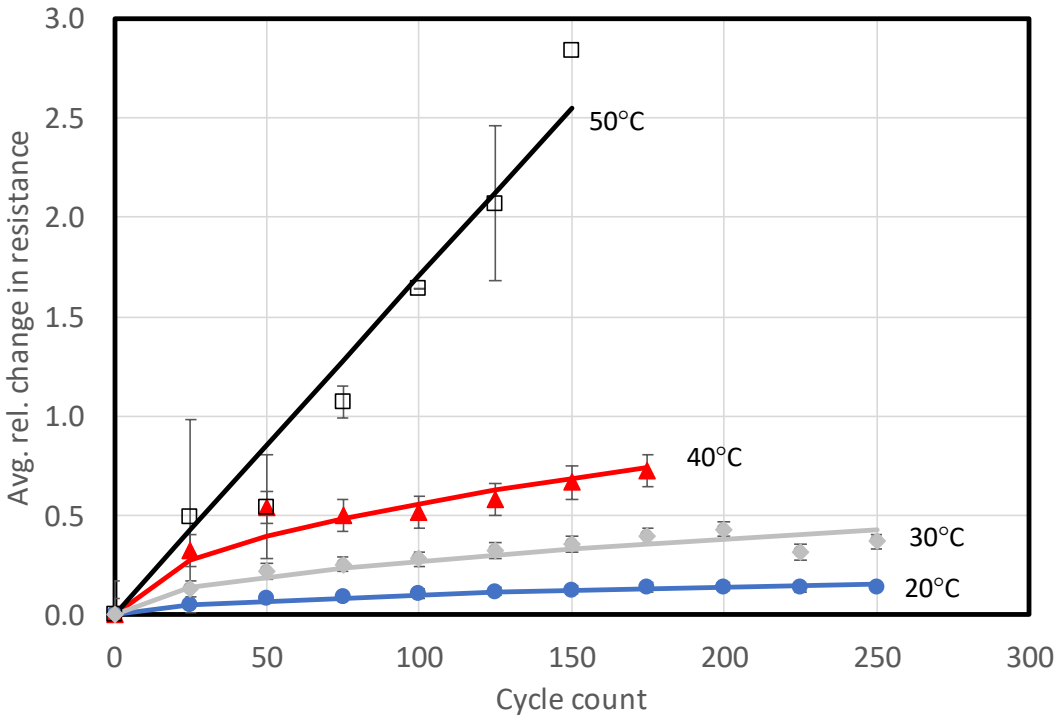

Figure 6a. Average, relative change in cell resistance as a function of cycle count and test temperature for the high-porosity cells. The markers represent the average, relative values and the curves, the results of fitting. The error bars represent the range of values.

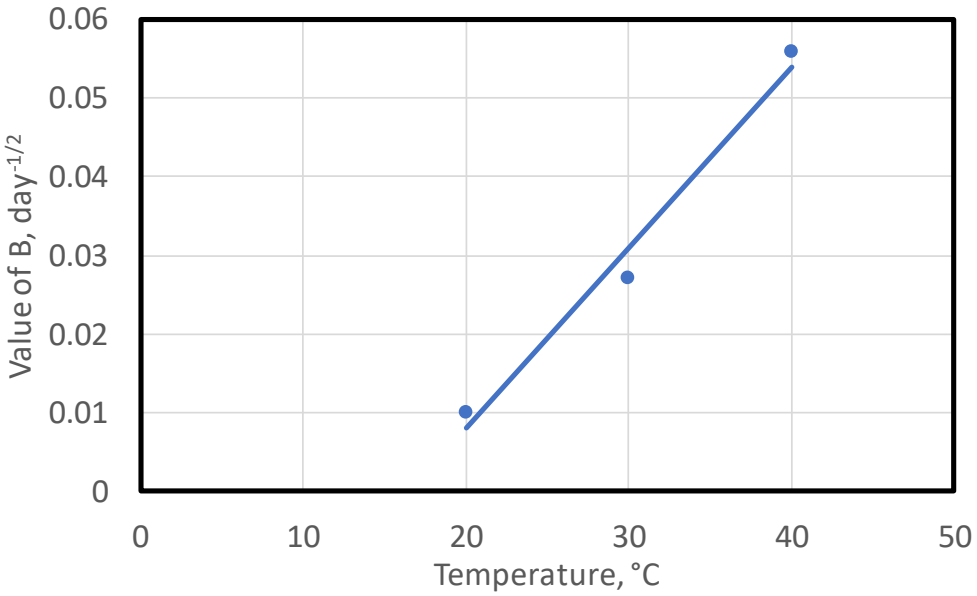

Figure 6b. Value of the fitting constant, *B*, vs. temperature. Least-squares fitting of these data produced a value of r^2 of 0.98.

Table 6. Values of the fitting constants, *A* and *B*, for the values of average, relative resistance from the high porosity cells.

Temperature, °C	*A*, $(count)^{-1}$	*B*, $(count)^{-1/2}$	r^2
20	--	1.00×10^{-2} (2.56×10^{-4})	0.99
30	--	2.70×10^{-2} (1.21×10^{-3})	0.98
40	--	5.59×10^{-2} (2.56×10^{-3})	0.99
50	1.70×10^{-2} (8.22×10^{-4})	--	0.99

Post-test analysis. After 5 cycles, one cell from each test condition was removed and analyzed for physical changes on the anode. Figure 7a shows optical photographs of the anodes from these cells. Examining the photographs in Figure 7a shows that lithium plating was present in cells tested at 20 and 30°C, but not in those tested at higher temperatures regardless of porosity. Apparently, porosity did not play an important part in lithium plating at this stage of cell aging. Temperature did.

With additional cycling, the lithium deposits increased in size, as shown in Figure 7b, for the cells tested at 20 and 30°C. Evidence of lithium plating was clearly seen at 40°C regardless of porosity. It was not discernable whether the deposit on the low porosity anode was larger than that on the high porosity anode in terms of total area covered and deposit thickness. There seemed to be evidence of the start of lithium plating at 50°C after 200 cycles. Adding these

observations to those above leads one to conclude that the porosity of the negative electrode had a minor part in delaying lithium deposition; temperature had the major effect.

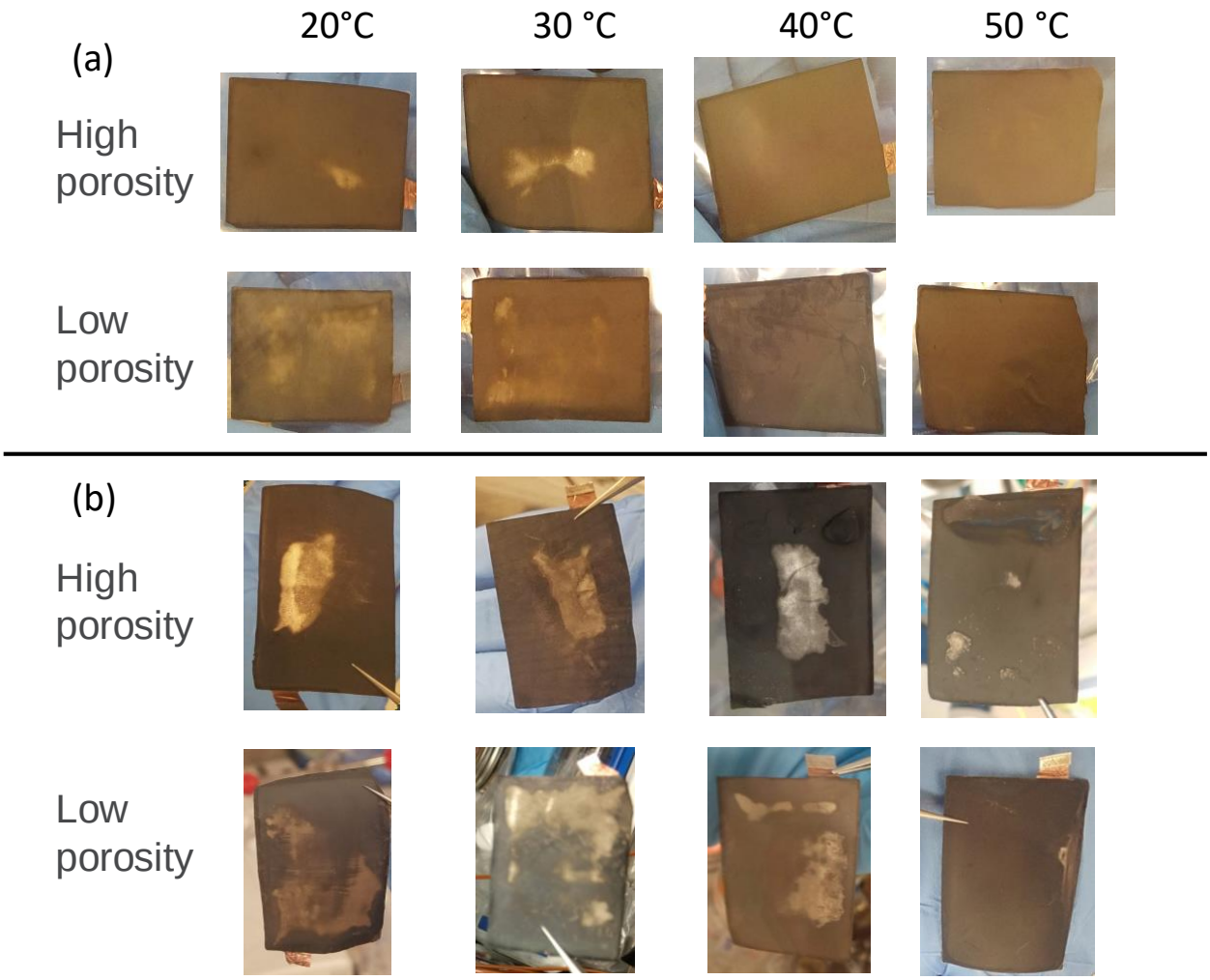

Figure 7. Glove box images of the negative electrodes (a) after 5 fast-charge cycles and (b) at the end of fast-charge testing as a function of temperature and porosity.

Model predictions for lithium plating during initial fast charging. The electrochemical model was used to investigate the effect of temperature and anode porosity on lithium plating and electrolyte depletion during initial cycling. Example results are shown in Figure 8. Commensurate with visual observations shown in Figure 7, the model predicts significant amounts of lithium plating except for cells operating at 50°C. Increasing temperature significantly mitigates lithium plating due to improvements in the electrolyte transport properties[12,13, 30] and graphite transport/kinetic properties. Further model development is required to better understand the reversibility of the lithium stripping process and the effect of this on cell lifetime.

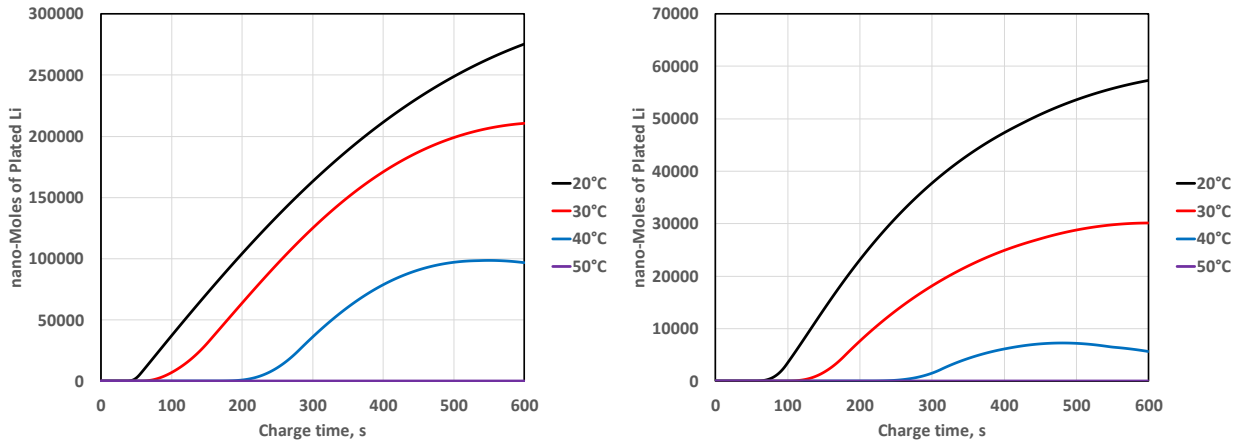

Figure 8. Model predictions for plated lithium during 10-minute CC-CV charging for cells with low porosity (left) and high porosity (right) anodes. Note that 12,000 nanomoles of lithium capacity corresponds to 1% of the cell capacity.

In summary, the modeling suggests that higher anode porosity should mitigate lithium plating more than experimentally observed. Continued research is needed to better understand these phenomena. Possible explanations include:

- Lithium stripping is less reversible for the higher porosity case.
- Plating for the high porosity case is driven by local heterogeneity, which is challenging to model, instead of bulk transport limitations.
- Uncertainty in effects of carbon/binder domain on transport/kinetic processes
- Plating is driven more by limitations in the intercalation process than liquid phase ionic transport.
- The continued growth of metallic lithium is very different than the initial plating behavior.
- Lithium plating is a highly stochastic process that is not well represented with the standard deterministic approach reported here.

The reader should note some uncertainty in the microstructure properties selected for the anode. Similar plating predictions for the high porosity case were obtained with a higher value of tortuosity of 6.5 and a particle radius of 4 μm. These values were used for the calendered anode. When the model for the high porosity anode was run with the reconstruction prediction for a tortuosity factor of ~3, no lithium plating was predicted for the tested temperatures except 20°C. Also, when the specific surface area for the high porosity model was not reduced by 50% from the standard value, as described in the supplemental material, significantly less amounts of plating were predicted for the cell with the high porosity anode. Thus, the microstructure

properties in the model for the high porosity anode had to be made more restrictive to transport and kinetics than expected to match experimental observations for lithium plating. Another possibility is that local heterogeneity instead of bulk transport limitations was driving plating for the high porosity anode, which was neglected in the pseudo-2D electrochemical model.

SEM imaging of the uncalendered and calendered graphite electrodes (see Figure 9) revealed high porosity electrodes were more heterogenous due to a combination of a wider pore size distribution and a more heterogenous carbon-binder domain (CBD) spatial distribution. Specifically, some large pores were obstructed with CBD, which means there was less CBD left for the smaller pores, which could produce poorly connected or isolated particles for the high porosity electrodes, leading to low local conductivity. This agreed with direct measurements of conductivity performed on various electrodes, revealing significant, in-plane heterogeneities,[31] which were attributed to microstructure heterogeneity and porosity dependence, with higher conductivities for low porosity electrodes.[32] Mesoscale electrochemical modeling predicted electrode microstructure inhomogeneity, and this gave rise to localized plating that occurred both earlier (at ~24 s) and more severely (~twice) compared with homogeneous electrodes during fast charging.[33]

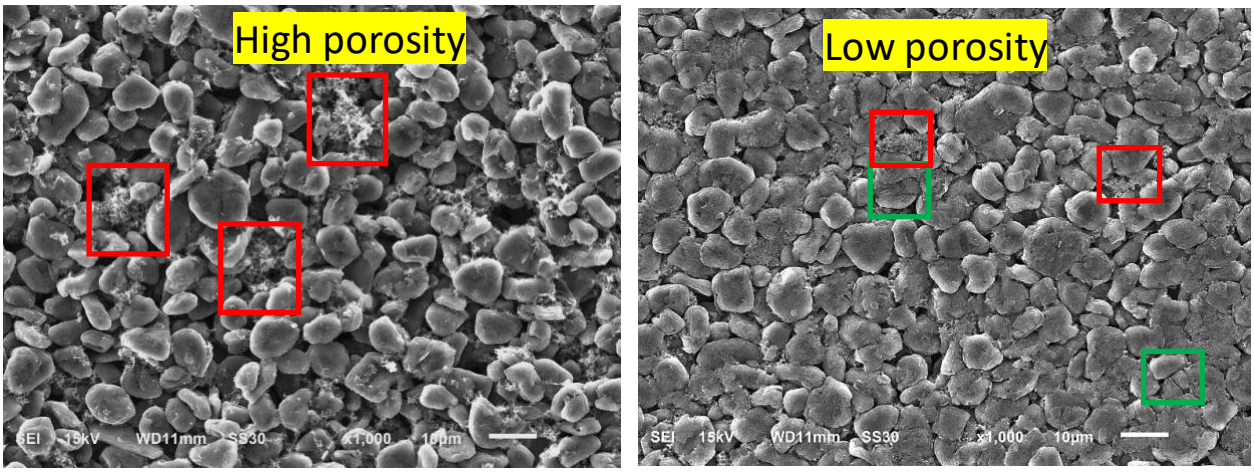

Figure 9. SEM images of the cross-sections of the high- and low-porosity electrodes (1000×). The red rectangles indicate carbon-binder domains, and the green ones, cracked particles

Figure 10a illustrates how the characteristic ionic diffusion time is shorter for the high porosity electrodes, even though the calendered electrodes are thinner, with difference increasing with decreasing ionic transport coefficient. Figure 10b generalizes the approach to different porosities, considering doublets (thickness, theoretical porosity) that preserve the active material theoretical capacity (cf. Figure 10c). Only electrodes that had a very low value of the coefficient α ($\tau = \varepsilon^{1-\alpha}$) and that were moderately calendered (top left region of Figure 10b) had a lower diffusion time as compared to that of the uncalendered electrode. This result suggests that calendering electrodes exhibiting poor-to-intermediate ionic diffusion will aggravate ionic transport limitations with a stronger negative impact for thinner electrodes.

Microstructure analysis of the specific surface area revealed the analytical prediction not to be accurate for the low porosity case, with significantly lower surface area for the calendered area than initially expected (see Figure 11). The theoretical relationship is following the correct trend only for the moderate to high porosity (>0.4), with the discrepancy decreasing with porosity. The

error for the low porosity region is expected as the theoretical relationship is monolithically decreasing with the porosity, thus predicting a maximum surface area for a zero porosity. This is obviously wrong as there can't be any interface in a one phase medium. A correct theoretical specific surface area – porosity relationship should predict a zero surface area for the two extremes point (zero-porosity and unit porosity), thus implying the function is first increasing, reaching a maximum when active material and pore volume fractions are identical, and then decreasing with porosity.

In summary, the modeling suggests that the calendered electrode has only slightly better kinetics (specific surface area was only slightly higher and less than expected); significantly poorer ionic diffusion (higher characteristic diffusion time even though the electrode was thinner); and shorter solid-state diffusion time (which should delay lithium plating). The reader is invited to read the supplemental material for a more thorough discussion about the impact of calendering on microstructure.

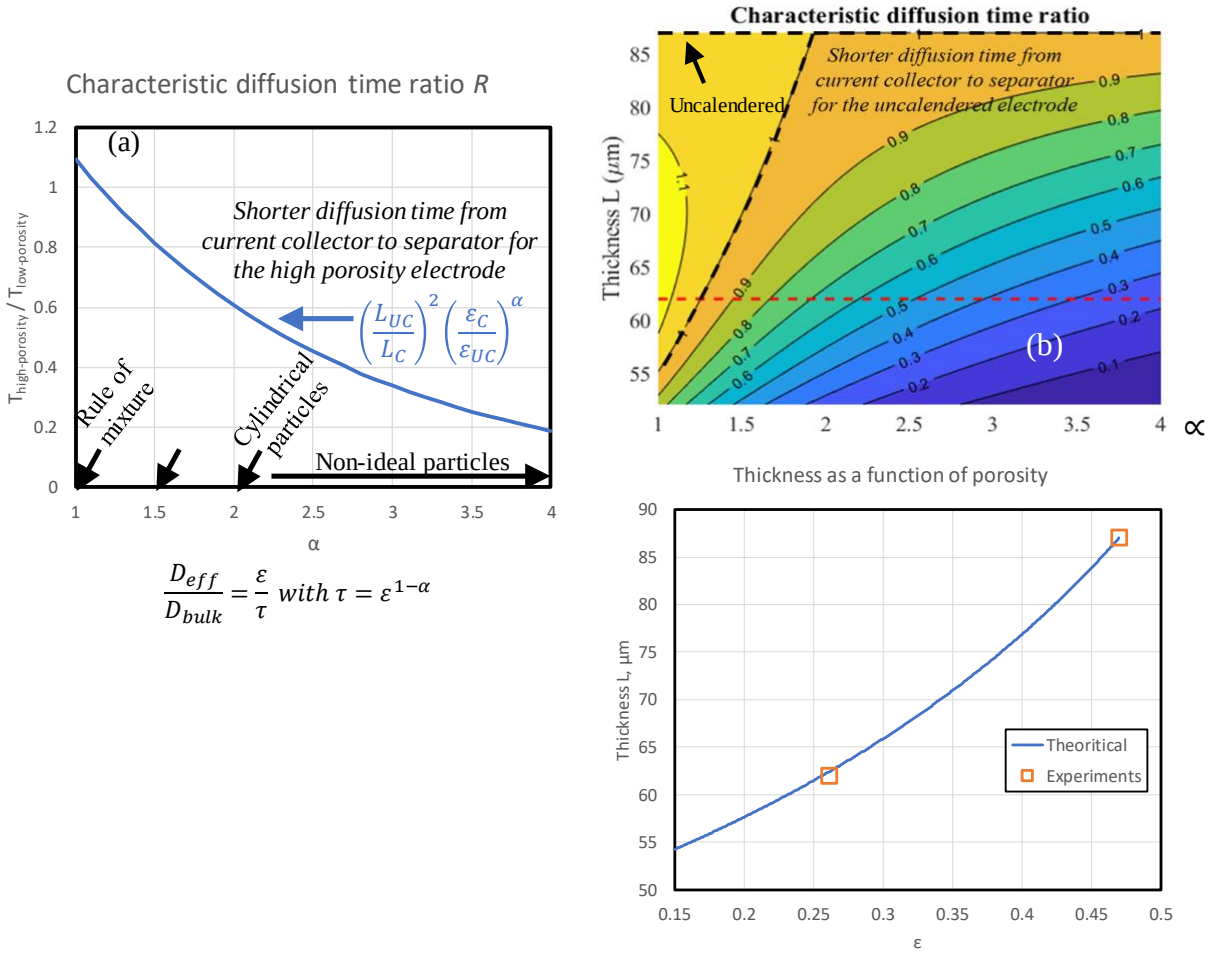

$$\frac{D_{eff}}{D_{bulk}} = \frac{\varepsilon}{\tau} \; with \; \tau = \varepsilon^{1-\alpha}$$

Figure 10. Characteristic diffusion time ratio, *R*, between (a) the high and low porosity electrodes that were experimentally tested and (b) the high and a range of low porosity electrodes considering various calendered thicknesses (dashed black line represents the characteristic diffusion isovalue time, and the red dashed line corresponds to the thickness of the calendered electrode). (c) Electrode thickness as a function of porosity from an uncalendered electrode. See the supplemental material for model details.

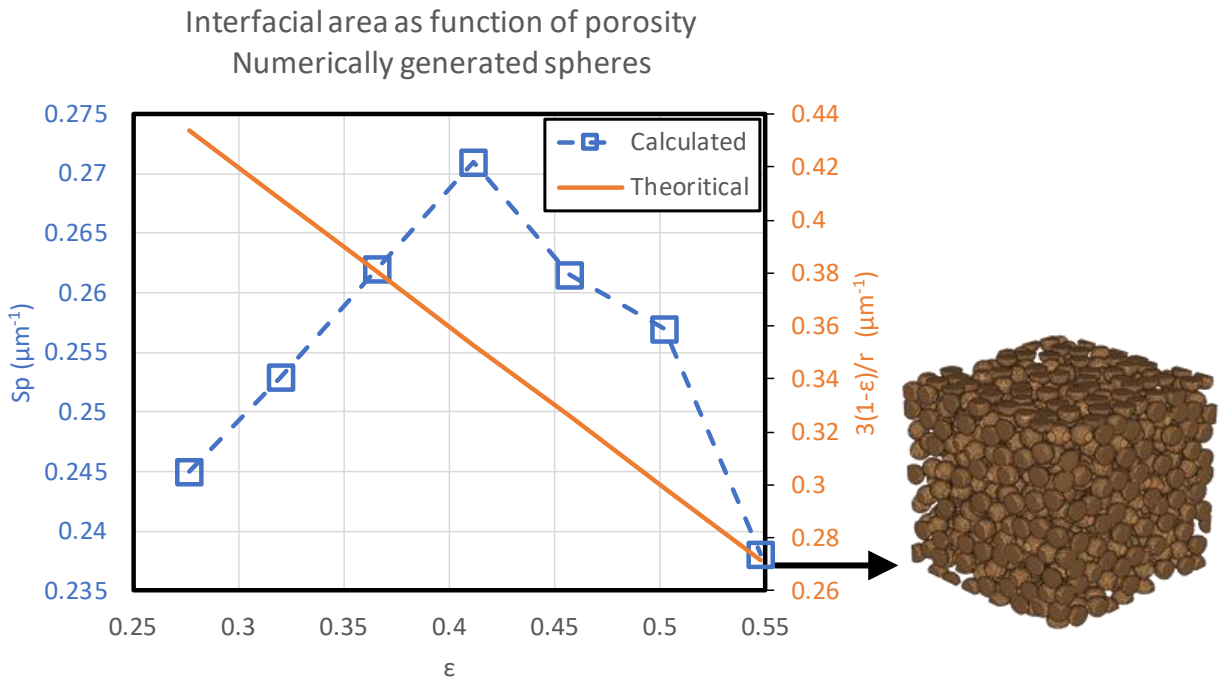

Figure 11. Interfacial specific area as function of porosity. Void volume fractions range from 0.277 to 0.548, which would correspond to porosities from 0.2 to 0.5 if the additives were considered.

The model was also used to provide insight into how temperature and anode porosity affect liquid-phase ion transport. Figure 12 illustrates model predictions for the lithium salt concentration in electrolyte 100 seconds into a 10-minute charge. During charge, lithium ions move from the cathode into the anode. Thus, the salt concentration increases near the cathode and decreases in the anode due to the applied current. Note, all simulations start with a uniform salt concentration of 1.2 M and the average salt concentration for all cases throughout simulations are 1.2M due to conservation of lithium ions in electrolyte.

For the low porosity cell, severe electrolyte depletion was predicted for all temperatures except 50°C. The high porosity cell exhibited less electrolyte depletion in the anode, and the anode was predicted to be used more uniformly compared to the low porosity case. This finding is explained by the smaller characteristic diffusion time of the high porosity electrodes, even though the low porosity electrodes were thinner (cf. Figure 10a). The electrolyte salt profile resulted in electrodes being preferentially used near the separator as compared to close to the current collectors. For instance, 300 seconds into charging at 20°C, the average intercalation fraction for the low porosity anode is predicted to be 0.95 near the separator and only 0.04 near the current collector. Conversely, these values for the high porosity anode are 0.75 and 0.11, respectively. The high porosity cell displayed lithium plating at 40°C, even though severe electrolyte depletion was not predicted. There is still a strong gradient in the predicted intercalation fraction, varying from 0.85 to 0.21 from the separator to current collector. For the high porosity cases at 20-40°C, plating was exacerbated by electrolyte transport limitations but was also driven by limitations in lithiating particles with larger radius/less surface area.

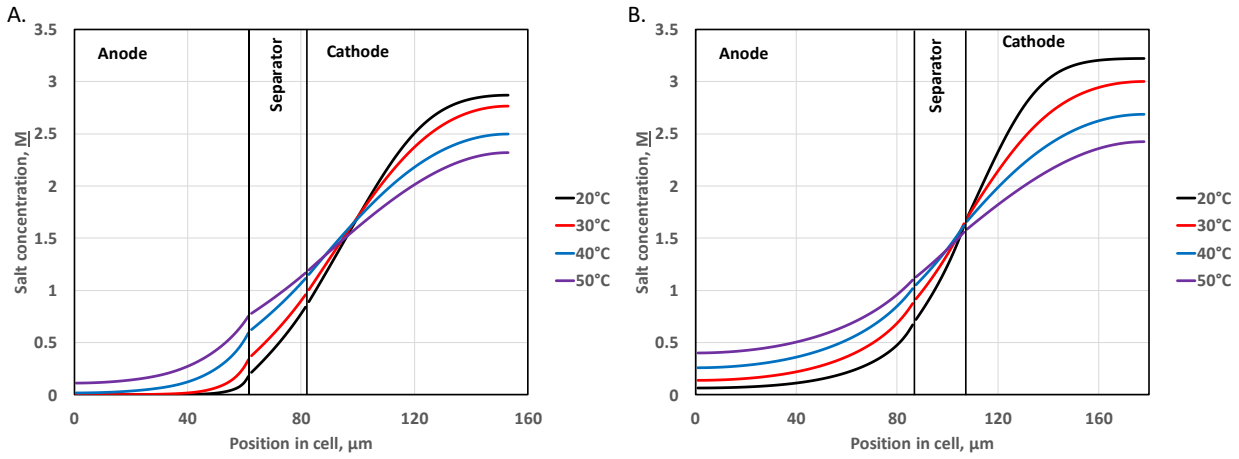

Figure 12. Model predictions for salt concentration 100 seconds into 10 minute CC-CV charging for cells with low porosity (A) and high porosity (B) anodes. The cell thickness for the low porosity and high porosity anodes are 153 microns and 178 microns, respectively.

Discussion

The results indicate that the porosity of the graphite electrode in these experiments played a relatively small role in limiting lithium deposition. Both at short and long times, temperature seemed to determine the extent of lithium plating. At high temperatures, lithium plating was not seen at short times and was limited at longer ones.

The fact that anode porosity did not significantly reduce the amount of lithium plating is not well explained by current models. Microstructure parameters for the high porosity cell had to be made more restrictive to transport and kinetics than expected to match experimental capacities and to predict significant amounts of plating. A plausible explanation lies in the high uncertainty of the representation of the carbon and binder additives. Since the additive phase is very difficult to image, several groups[34,35] have tried to numerically generate it by various approaches. Their results indicate that, depending on how this phase is distributed within the pore, its impact on the tortuosity factor varies significantly. While such work can be used to predict the tortuosity factor, they did not explore the whole design space of the additive phase, implying that their results may still underestimate its actual impact on diffusion. The fact that lithium plating was not significantly reduced with the high anode porosity seems to be due to anode tortuosity being unexpectantly high. It also strongly challenges the common assumption used in battery macromodels that tortuosity varies exponentially with porosity. Microstructure analysis also revealed that the standard analytical correlation between specific surface area and porosity is not

valid for the low porosity electrodes. Lastly, the impact of calendering on solid-state characteristic diffusion time was compensated by slightly decreasing the particle size to avoid overfitting the other microstructure parameters, especially the tortuosity factor. The results summarized in this paper highlight the fact that more research needs to be done to definitively determine how microstructure properties change with electrode porosity.

The porosity of the electrode did have a marked effect on performance degradation, however. The apparent kinetic rates for capacity decline for the both types of cells in the range of 20-40°C tended to be based on parabolic ($t^{1/2}$) kinetics, with a relatively small contribution from a linear-with-time process. It was curious to see that, at 50°C, this tendency remained true in the low porosity cells. On the other hand, the high porosity cells at this high temperature displayed a very different rate law. At first, it was thought that logistics kinetics were caused by the "consumption" of a resource, such as the loss of active material due to a process, like the reaction of plated lithium with the binder. If this were true, evidence of delamination should have been seen. From the above results, it was not, leaving the source of the observation to remain the subject of future inquiry.

The change in apparent rate laws was more obvious in those for resistance increase. Here, the rate law was primarily linear with time for the low porosity cells and parabolic for the high porosity ones. Cell resistance can be attributed to many factors, such as liquid-phase transport limitations to and from the reaction site; diffusion in the active materials; and reaction kinetics.

Since resistance increase in lithium-ion cells has been attributed to many factors, including SEI layer growth,[36-38] it is interesting to see how surface area affected the overall resistance growth mechanism. In the high porosity case where surface area would be expected to be plentiful, if the overall electrochemical kinetics do not markedly change, the change in the cell resistance may be attributable to other factors. Of these, changes in the rate of ionic diffusion through the solids would be expected to be the major contributor to resistance change. Thus, the observed rate laws may indicate that ionic diffusion was more hindered in the high porosity case, leading to the inference that there was more SEI layer growth in this case due to the higher surface area. This is a reasonable because parabolic kinetics are often associated with pseudo-one-dimensional diffusion, such as that through an SEI layer.[30, 36-39]

Electrochemical modeling suggests that other loss mechanisms besides lithium plating become more dominant at elevated temperatures, such as loss of positive or negative active material. Although not modeled, losses from SEI growth not associated with lithium plating are expected to increase significantly with temperature,[23] which may or may not grow as a function of the square root of time. The effect of operating temperature on other fast charge degradation mechanisms, such as cathode particle cracking, is not well understood. The reported model cannot explain why the capacity and resistance behavior with cycling for the high porosity anode at 50°C was very different from all other test conditions. Detailed modeling of these other mechanisms and a more fundamental understanding of lithium plating/striping reversibility are important and will be the subject of future work.

Note that the low porosity anode has a total energy density of 215 Wh kg^{-1} (not considering packaging/current collector tabs, as well as extra edge material/electrolyte), and that for the 47% porous anode cell is less, 200 Wh kg^{-1}. The volumetric energy densities were 560 and 485 Wh L^{-1} for cells containing low and high porosity anodes, respectively. Overall, increasing porosity appears not to be a very effective strategy for delaying plating, less than the modeling would have suggested, especially given the decreases in total cell energy density. Instead engineering of specific architecture features, such as micron size holes or channels, seems more promising. [40, 41] Laser ablation[42] and incorporation of pore formers[43] are two effective methods for introducing these features for fast lithium-ion transport within the electrolyte phase.

Conclusion

We tested two sets of small pouch cells in the temperature range of 20 to 50°C, one set contained low porosity graphite electrodes and the other, high porosity ones, using a fast-charge cycling protocol. After five, fast-charge cycles, regardless of porosity, the cells tested at 40 and 50°C displayed no observable lithium deposits; the cells tested at lower temperatures did. After 200 cycles, some lithium deposits were seen in all cells, with less lithium on the graphite electrodes in the cells tested at higher temperatures.

Porosity, however, did have a marked effect on the kinetics of performance decline. The apparent kinetic rates for capacity decline for the both types of cells in the range of 20-40°C tended to be based on parabolic ($t^{1/2}$) kinetics, with a relatively small contribution from a linear-with-time process. The capacity loss data in the low porosity cells at 50°C followed this trend.

However, the capacity loss data in the high porosity cells at this temperature did not. Instead, these data displayed logistics kinetics. The apparent rate laws for changes in cell resistance was primarily linear with time for the low porosity cells and parabolic for the high porosity ones.

A set of modeling tools has been used to help interpret the effect of anode porosity and ambient temperature on fast charge performance. The effect of temperature on lithium plating and initial cell capacity observed matches well with model predictions. Lithium plating is mitigated with elevated temperature due to enhanced ionic transport and kinetics. The observed effect of anode porosity on lithium plating is not well matched by model simulations, which suggest that increasing anode porosity should reduce the amount of lithium plating. Possible explanations are discussed, including the need to better understand the variations in microstructure properties with porosity and carbon-binder domain effects. The results presented illustrate the need to incorporate other degradation mechanisms, such as mechanical breakdown/SEI changes, into detailed electrochemical modeling to better understand fast charge performance.

Acknowledgments

We gratefully acknowledge support from the U. S. Department of Energy (DOE), Vehicle Technologies Office, specifically from Samuel Gillard, Peter Faguy, and David Howell. Argonne National Laboratory is operated for DOE Office of Science by UChicago Argonne, LLC, under contract number DE-AC02-06CH11357. This work was authored in part by the National Renewable Energy Laboratory, operated by Alliance for Sustainable Energy, LLC, for the U.S. Department of Energy (DOE) under Contract No. DE-AC36-08GO28308. The views expressed in the article do not necessarily represent the views of the DOE or the U.S.

Government. The electrodes and pouch cells used in this article were made by Argonne's Cell Analysis, Modeling and Prototyping (CAMP) Facility, which was supported by the Applied Battery Research for Transportation Program.

AUTHOR INFORMATION

Corresponding Author

*E-mail: ira.bloom@anl.gov

ORCID

Ira Bloom: 0000-0002-4877-473X

Francois Usseglio-Viretta: 0000-0002-7559-8874

Andrew Colclasure: 0000-0002-9574-5106

Zhenzhen Yang: 0000-0002-1073-3799

References

1. M. Inaba, H. Yoshida, Z. Ogumi, T. Abe, Y. Mizutani, M. Asano, *J. Electrochem. Soc*., 142 (1995) 20-26.

2. A. Funabiki, M. Inaba, T. Abe, Z. Ogumi, *J. Electrochem. Soc*., 146 (1999) 2443-2448.

3. G.-A. Nazri and G. Pistoia, eds., Lithium Batteries: Science and Technology, Springer Science+Business Media, New York, 2009.

4. T. Enoki, M. Suzuki, M. Endo, Graphite Intercalation Compounds and Applications, Oxford University Press, New York, 2003.

5. S. S. Zhang, *J. Power Sources*, 161 (2006) 1385–1391.

6. J. C. Burns, D. A. Stevens, J. R. Dahn, *J. Electrochem. Soc*., 162 (2015) A959–A964.

7. S. S. Zhang, K. Xu, T. R. Jow, *J. Power Sources*, 160 (2006) 1349–1354.

8. M. Petzl, M. Kasper, M.A. Danzer, *J. Power Sources*, 275 (2015) 799-807.

9. S. Tippmann, D. Walper, L. Balboa, B. Spier, W.G. Bessler, *J. Power Sources*, 252 (2014) 305-316.

10. X. Sun, X. Zhang, K. Wang, N. Xu, Y. Ma, J. Solid State Electrochem., 19 (2015) 2501-2506.

11. T. Waldmann, B. I. Hogg and M. Wohlfahrt-Mehrens, J. Power Sources, 384 (2018) 107-124.

12. A. M. Colclasure, A. R. Dunlop, S. E. Trask, B. J. Polzin, A. N. Jansen, and K. Smith, *J. Electrochem. Soc.*, 166 (2019) A1412-A1424.

13. A. M. Colclasure, T.R. Tanim, A.N. Jansen, S.E. Trask, A.R. Dunlop, B.J. Polzin, I. Bloom, D. Robertson, L. Flores, M. Evans, E.J. Dufek, and K. Smith, *Electrochimica*

Acta, 337 (2020) 135854.

14. M. Doyle and J. Newman, *Electrochimica Acta*, **40** (1995) 2191-2196.

15. K. Smith and C.-Y. Wang, *J. Power Sources*, **160** (2006) 662–673.

16. C. Fear, T. Adhikary, R. Carter, A.N. Mistry, C.T. Love, and P.P. Mukherjee, ACS. *Appl. Mater. Interfaces*, **12** (2020) 30438-30448.

17. M-T F. Rodrigues, I.A. Shkrob, A.M. Colclasure, D.P. Abraham, J. *Electrochem Soc.*, **167** (2020) 130508.

18. B.S. Vishnugopi, A. Verma, and P.P. Mukherjee, *J. Electrochem. Soc.*, **167** (2020) 090508.

19. Cell Analysis, Modeling and Protoyping.

20. T. R. Tanim, E. J. Dufek, M. Evans, C. Dickerson, A. N. Jansen, B. J. Polzin, A. R. Dunlop, S. E. Trask, R. Jackman, I. Bloom, Z. Yang, and E. Lee, *J. Electrochem. Soc.*, 166, A1926-A1938 (2019)

21. Battery Test Manual For Plug-In Hybrid Electric Vehicles, Rev. 3, September 2014, INL/EXT-14-32849.

22. https://wstein.org/edu/winter06/20b/notes/html/node59.html.

23. D. Ren, K. Smith, D. Guo, X. Han, X. Feng, L. Lu, M. Ouyan, and J. Li. *J. Electrochem. Soc.*, 165 A2167-A2178 (2018).

24. E. J. McShane, A. M. Colclasure, D.E. Brown, Z. M. Konz, K. Smith, B. D. McCloskey, *ACS Energy Letters*, 5 (2020) 2045-2051.

25. M. Klett, J. A. Gilbert, S. E. Trask, B. J. Polzin, A. N. Jansen, D. W. Dees, and D. P. Abraham, *J. Electrochem. Soc.*, 163 (2016) A875-A887.

26. D. P. Abraham, S. D. Poppen, A. N. Jansen, J. Liu, and D. W. Dees, *Electrochimica*

Acta, 49 (2004) 4763-4775.

27. F.L.E. Usseglio-Viretta, A. Colclasure, A.N. Mistry, K.P.Y. Claver, F. Pouraghajan, D.P. Finegan, T.M.M. Heenan, D. Abraham, P.P. Mukherjee, D. Wheeler, P. Shearing, S.J. Cooper, and K. Smith, *J. Electrochem. Soc*., 165 (2018) A3403-A3426.

28. J. Landesfeind, J. Hattendorff, A. Ehrl, W.A. Wall, and H.A. Gasteiger, *J. Electrochem. Soc*., 163 (2016) A1373-A1387.

29. The decomposition of the rate law, $y=At^z$, where $0.5 < z < 1.0$, into $y=Bt + Ct^{1/2}$ can be easily demonstrated by performing linear regression analysis on calculated data. For example, the equation, $y=(8.35 \times 10^{-4})t + (7.21 \times 10^{-3})t^{1/2}$, was obtained from using the LINEST function in Microsoft® Excel® using the data calculated from $y=(5 \times 10^{-3})t^{0.75}$. Similar results can be obtained from other values of z. In the example used, the value of r^2 was greater than 0.99, and the standard error in the coefficients were 1.97×10^{-5} and 2.17×10^{-4}, respectively.

30. X. Yang, G. Zhang, S. Ge, and C-Y Wang, *Proc. Natl. Acad. Sci. Unit. States Am*., 115 (2018) 7266-7271.

31. B. J. Lanterman, A. A. Riet, N. S. Gates, J. D. Flygare, A. D. Cutler, J. E. Vogel, D. R. Wheeler, and B. A. Mazzeo, *J. Electrochem. Soc*, 162 (2015) A2145-A2151.

32. S. W. Peterson and D. R. Wheeler, *J. Electrochem. Soc*, 161 (2014) A2175-A2181.

33. A. Mistry, F. L. E. Usseglio-Viretta, A. Colclasure, K. Smith, and P. P. Mukherjee, *J. Electrochem. Soc.*, 167 (2020) 090542.

34. A. N. Mistry, K. Smith, and P. P. Mukherjee, ACS Appl. Mater. Interfaces, 10 (2018), 6317-6326

35. S. Hein, T. Danner, D. Westhoff, B. Prifling, R. Scurtu, L. Kremer, A. Hoffmann, A. Hilger, M. Osenberg, I. Manke, M. Wohlfahrt-Mehrens, V. Schmidt, and A. Latz, J. Electrochem. Soc., 167, 013546 (2020)

36. G. Blomgren, *J. Power Sources*, **81-82** (1999) 112-118.

37. K. Amine, M. J. Hammond, J. Liu, C. Chen, D. W. Dees, A. N. Jansen, and G. L. Henriksen, Proc. of the 10th Int. Meeting on Lithium Batteries, Como, Italy, May 28-June 2, 2000, p. 332 (2000).

38. I. Bloom, B. W. Cole, J. J. Sohn, S. A. Jones, E. G. Polzin, V. S. Battaglia, G. L. Henriksen, C. Motloch, R. Richardson, T. Unkelhaeuser, D. Ingersoll, and H. L. Case, *J. Power Sources* 101 (2001) 238-247.

39. E. Strauss, D. Golodnitsky, and E. Peled, *Electrochemical and Solid State Letters*, **2** (1999) 115-117.

40. W. Mai, F. Usseglio-Viretta, A. Colclasure, K. Smith, *Electrochimica Acta*, 341 (2020) 136013.

41. F.L.E. Usseglio-Viretta ,W. Mai, A. Colclasure, M. Doeff, E. Li, and K. Smith, *Electrochimica Acta*, 341 (2020) 136034.

42. K-H Chen, M. J. Namkoong, V. Goel, C. Yang, S. Kazemiabnavi, S.M. Mortuza, E. Kazyak, J. Mazumder, K. Thornton, J. Sakamoto, N.P. Dasgupta, *J. Power Sources*, **471** (2020) 228475.

43. D.P. Singh, F.M. Mulder, A.M. Abdelkader, and M. Wagemaker, *Advanced Energy Materials* **3** (2013) 572-578.

Supplemental material.

Effect of anode porosity and temperature on performance and lithium plating during fast-charging of lithium-ion cells

David C. Robertson,[1] LeRoy Flores,[1] Alison R. Dunlop,[1] Stephen E. Trask,[1] Francois L. E. Usseglio-Viretta,[2] Andrew M. Colclasure,[2] Zhenzhen Yang,[1] and Ira Bloom[1]

[1]Chemical Sciences and Engineering Division

Argonne National Laboratory

9700 South Cass Avenue

Lemont, IL 60439 USA

[2]Center for Integrated Mobility Sciences

National Renewable Energy Laboratory

Golden, CO 80401 USA

Detailed Microstructure Analysis

Tortuosity factor and characteristic diffusion time. How effective increasing anode porosity is in improving fast charge behavior from improved liquid phase ion transport is highly dependent on corresponding changes to tortuosity. Unfortunately, the tortuosity factor is challenging to measure or calculate.[1] While its value can be bounded through careful error estimations, the

interval of confidence can be quite significant.[1] The porosity and tortuosity factor are used to calculate the effective transport properties for the electrolyte phase within the composite layers. Often, the tortuosity factor, τ, is calculated with the classical Bruggeman relationship, $\tau = \varepsilon^{-\alpha}$, where ε is the porosity, and the exponent, α, is usually set to 0.5, assuming spherical particles and high porosity,[2] which is often not valid for high-energy-density Li-ion electrodes. The tortuosity of the NMC electrodes with 35% porosity is estimated to be around three based on microstructure reconstructions, impedance measurements with blocking electrolyte, and electrochemical model fitting to cathode rate data.[1] The separator tortuosity for Celgard 2320 has been measured by Gasteiger and colleagues to be around 4.[3] Calendering not only reduces porosity but also rearranges particles within the electrode. Specifically, calendering aggravates particle misalignment, with the particle long diameter sitting orthogonal to the electrode thickness and effectively blocking even more of the ionic diffusion path, which results in an even higher tortuosity factor anisotropy ($\tau_{through\ plane} > \tau_{in-plane}$). Such a detrimental impact of calendering has been calculated on reconstructed electrodes in previous works both for graphite[1, 4] and NMC[1, 4, 5] electrodes. Therefore, a higher tortuosity factor is expected for the calendered graphite due to the combined impacts of reduced porosity and particle misalignment.

Based on microstructure reconstructions performed on other 1506T graphite anodes and the uncertainty induced by the additives,[1] we estimate that the tortuosity factor for the high porosity anode is between 2.5 and 3.3, and that for the low porosity anode is between 5.3 and 9.0. However, experimental techniques for estimating tortuosity sometimes suggest that high porosity anodes have much higher tortuosity than predicted from reconstruction techniques.[3] The discrepancy between techniques is not well understood but may be related to carbon/binder

additive effects on ionic transport. Most of the uncertainty in the microstructure characterization calculation is derived from the additives for which spatial distribution is difficult to obtain.[1] The tortuosity factors used in the electrochemical model are fitted to match experimental data in the results section and are compared with the expected values mentioned above.

Both calendered and uncalendered electrodes are equivalent in term of active material loading (9.94 mg cm^{-2}). While calendered electrodes are thinner but have a higher tortuosity factor, they are not necessarily equivalent with their uncalendered counterparts in term of characteristic diffusion time, $T = L^2/D_{eff}$ with L the electrode thickness and D_{eff} the effective ionic diffusion coefficient. The latter is related to the porosity, ε, the tortuosity factor, τ, and the bulk ionic diffusion coefficient, D_{bulk}, according to $D_{eff}/D_{bulk} = \varepsilon/\tau$. Assuming calendering only redistributes the location of particles without modifying their volume, the theoretical porosity, ε_C, of the calendered electrode for a given thickness, L_C, can be determined by following a one-dimensional analogy (electrode length = pore length + solid length).

$$\text{Uncalendered electrode} \quad \begin{matrix} L_{UC} = L_{UC,solid} + L_{UC,pore} \\ \text{with } L_{UC,pore} = \varepsilon_{UC} \times L_{UC} \end{matrix} \quad \text{then} \quad L_{UC,solid} = (1 - \varepsilon_{UC}) \times L_{UC}$$

$$\text{Calendered electrode} \quad \begin{matrix} L_C = L_{C,solid} + L_{C,pore} \\ \text{with } L_{C,pore} = \varepsilon_C \times L_C \end{matrix} \quad \text{then} \quad L_{C,pore} = \frac{\varepsilon_C \times L_{C,solid}}{1 - \varepsilon_C}$$

$$\text{and } L_{UC,solid} = L_{C,solid} \text{ (solid incompressible assumption)}$$

The characteristic diffusion time ratio, *R*, of the uncalendered over the calendered electrode can be then deduced, if both electrodes share the same tortuosity coefficients, α and γ, which is a standard assumption.

$$R = \frac{T_{UC}}{T_C} = \left(\frac{L_{UC}}{L_C}\right)^2 \left(\frac{\varepsilon_C}{\varepsilon_{UC}}\right)^{\propto} \text{ with } \tau = \gamma\varepsilon^{1-\alpha}$$

Particle diameter and solid-state characteristic diffusion distance. Anode particle morphology changes from calendering can have a significant impact on fast charge performance. Calendering slightly modifies particle morphology, inducing a more elongated, less spherical shape[6]. This morphology change, calculated for electrodes with higher porosities than the low porosity electrode of the present work [cf. Figure 28 of Reference 4], may be even stronger here. The resulting ellipsoids shape induces a shorter diffusion distance and a more uniform intercalation state in the particle volume. This can be modelled by reducing the particle equivalent diameter (set to 10 µm for the uncalendered electrodes), even though the particle volume is unchanged, to reflect the shorter diffusion distance. Open-porosity cracks also contribute to decrease the solid-state characteristic diffusion distance and has been observed for both calendered and un-calendered graphite.[1,7] Calendered-induced particle cracking has been observed for NMC electrodes,[8, 9] which indicates electrode crack density can increase with calendering. However, SEM images of the low- and high-porosity graphite electrodes (see Figure 10) did not reveal particle cracking, except locally. Such outcome is attributed to the much lower compression resistance[7] and Young modulus[10] of the graphite compared with NMC. Graphite being softer, calendering is more likely to alter its morphology rather than to induce defects or cracks.[6] Thus, calendering may reduce average solid-state transport distance (mostly from changes in particle morphology) and help to mitigate plating and improve fast charge capacity.

Specific surface area. Specific surface area has important implications on lithium consumption from lithium plating and solid-electrolyte interphase (SEI) growth. A high specific anode surface

area is beneficial for delaying plating but results in more lithium loss from SEI growth. Macroscopic models typically estimate the specific interfacial surface area, $3\varepsilon_s/R$, with ε_s the active material volume fraction and R the particle radius, assuming the particles are spherical with no surface roughness. However, the linear correlation between the interfacial surface area and the sphere volume fraction is only true for the high porosity region, due to the packing density limit. The decrease of interfacial area between the low and intermediate porosity electrodes is then not necessarily as low as expected. Likewise, the increase of effective current density between the low and intermediate porosity electrodes is not necessarily as high as expected.

To better understand the effect of porosity reduction from calendering on specific surface area for fast charge performance, the specific surface area was calculated for seven numerically generated, sphere-based microstructures using an available, open-source, stochastic algorithm,[11] and the results were compared with the theoretical values, $3(1-\varepsilon)/R$. Results are shown in Figure 12. Numerical values are corrected by a factor of 2/3 to take into account the surface area overestimation induced by a cuboid representation.[5, 12] Numerically calculated values are systematically lower compared with the analytical prediction, with a higher difference for the low porosity region (~ -44%) or a lower difference for the high porosity region (~ -15%). Such differences are due to the particle overlapping (mandatory to reach dense electrode) that tends to vanish for high porosity regions. While a decreasing trend is calculated for porosity larger than 0.41, interfacial specific surface area is increasing for smaller porosity. This result suggests that the low porosity electrode has a much smaller interfacial area than expected, only slightly higher than that of the uncalendered electrode. The analysis is relative, as absolute interfacial area is

likely to be higher than the values reported in Figure 12 due to particle surface roughness, non-spherical particles, and cracked particles. While surface roughness is expected to be similar between the uncalendered and calendered electrode, particle sphericity and crack density are expected to be lower and higher, respectively, for the calendered electrode, thus inducing a higher specific surface area for the low porosity electrode. More work is needed to quantify how specific surface area changes with porosity reduction from calendering and its impact on plating.

Internal cracking also provides more active surface area, with a significant contribution that can be expected for some heavily cracked graphite reported in the literature.[7] A few cracks were seen for the calendered graphite investigated in this work (see Figure 10); therefore, only a limited increase of surface area can be expected for the low porosity electrodes (specifically due to cracks). On the other hand, calendering induces an elongation of the graphite particles (as described in the previous paragraph) that results in a higher specific surface area. Indeed, ellipsoids or flake-like geometries have a higher surface area compared to a sphere of equivalent volume. To match the capacity/plating observations, the model was run with the specific surface area of the uncalendared electrode being half that of the classical value, $a_s = 3\varepsilon_s/r_p$. While the exact value was fitted, the trend was expected: the relationship specific surface area and porosity was not identical for the low and high porosity electrodes, with higher specific surface area for the calendered electrodes (at equivalent porosity with the uncalendered electrodes) due to particle morphology change. More work is needed to understand how tortuosity, effective particle size, and surface area vary with porosity as it is critical to designing high loading electrodes for fast charge performance.

References

1. F.L.E. Usseglio-Viretta, A. Colclasure, A.N. Mistry, K.P.Y. Claver, F. Pouraghajan, D.P. Finegan, T.M.M. Heenan, D. Abraham, P.P. Mukherjee, D. Wheeler, P. Shearing, S.J. Cooper, and K. Smith, *J. Electrochem. Soc*., 165 (2018) A3403-A3426.
2. B. Tjaden, S. J. Cooper, D. J. L. Brett, D. Kramer, and P. R. Shearing, *Current Opinion in Chemical Engineering*, 12 (2016) 44-51.
3. J. Landesfeind, J. Hattendorff, A. Ehrl, W.A. Wall, and H.A. Gasteiger, *J. Electrochem. Soc*., 163 (2016) A1373-A1387.
4. F. L. E. Usseglio-Viretta, D. P. Finegan, A. Colclasure, T. M. M. Heenan, D. Abraham, P. Shearing, and K. Smith, *J. Electrochem. Soc*., 167, (2020) 100513.
5. F. L. E. Usseglio-Viretta and K. Smith, *ECS Transactions*, 77 (2017) 1095-1118.
6. T. Günther, D. Schreiner, A. Metkar, C. Meyer, A. Kwade, and G. Reinhart, Energy Technol. 8 (2020) 1900026
7. C. Meyer, H. Bockholt, W. Haselrieder, and A. Kwade, J. Mater. Process. Technology, 249 (2017) 172-178.
8. M. Ebner, F. Geldmacher, F. Marone, M. Stampanoni, and V. Wood, Adv. Energy Mater., 3 (2013) 845-850
9. H. Bockholt, M. Indrikova, A. Netz, F. Golks, and A. Kwade, J. Power Sources, 325 (2016) 140-151

10. R. Koerver, W. Zhang, L. D. Biasi, S. Schweidler, A. O. Kondrakov, S. Kolling, T. Brezesinski, P. Hartmann, W. G. Zeier, and J. Janek, Energy Environ. Sci., 11 (2018) 2142-2158.

11. T. Waldmann, B. I. Hogg, and M. Wohlfahrt-Mehrens, J. Power Sources, 384 (2018) 107-124.

12. MATBOX: Microstructure Analysis Toolbox, https://github.com/NREL/MATBOX_Microstructure_analysis_toolbox

13. D. A. Rajon, P. W. Patton, A. P. Shah, C. J. Watchman, and E. Bolch, *Med. Phys.*, 29 (2002) 682-693.